ELSEVIER

Contents lists available at ScienceDirect

Electric Power Systems Research

journal homepage: www.elsevier.com/locate/epsr





Cooperative fault management for resilient integration of renewable energy[★]

Wenfeng Wan ^a, Peng Zhang ^{a,*}, Mikhail A. Bragin ^b, Peter B. Luh ^b

- ^a Department of Electrical and Computer Engineering, Stony Brook University, Stony Brook, NY 11794, USA
- ^b Department of Electrical and Computer Engineering, University of Connecticut, Storrs, CT 06269, USA

ARTICLE INFO

Keywords:
Cooperative fault management
Solar energy
Wind energy
Software-defined control
Distributed and asynchronous optimization
Real-time digital simulation

ABSTRACT

Cooperative fault management (CFM) is designed herein to control different types of renewable energy resources cooperatively during electrical faults. This paper studies systems with a high penetration of photovoltaic (PV) energy and wind energy. First, CFM leverages power converters of PV farms to boost the ride-through capability of nearby doubly-fed induction generators (DFIGs). By controlling PV farms' output voltages to change smoothly during both fault initiation and fault clearance, the widely used crowbar in DFIGs is less likely to be activated. Crowbar activation adversely makes DFIGs lose controllability and absorb reactive power. The second contribution is the development of a software-defined CFM controller and a controller-in-the-loop demonstration of the real-time performance of this optimization-based CFM. CFM capitalizes on distributed optimization formulation to enable flexibility, plug-and-play, and privacy-preserving. Computation time, however, is a major concern for optimization-based dynamics control. Real-time controller-in-the-loop simulation results show optimization-based CFM can output reference values around 60 ms and is quick enough for dynamic control.

1. Introduction

Renewable energy resources, e.g., solar and wind, are being promoted and invested aggressively by governments and corporations to achieve less ecological footprint and to facilitate distributed generation [1]. New York State has set the target of achieving 70% renewable energy by 2030, and for Hawaii, the target is 100% by 2045 [2].

Fault management for renewable energy resources is crucial for its integration but remains a knotty issue. The tripping of a large amount of wind energy after faults caused by lightning strikes led to the large-scale blackout in London, August 2019 [3]. Electrical faults as a result of wildfire resulted in the cessation of nearly 1,200 MW of solar photovoltaic (PV) generation in Southern California, June 2016 [4].

A key component of fault management is the fault ride-through capability, for which many entities have published their own standards and recommendations [5,6]. All entities have required renewable resources to keep connected to the grid for a certain period instead of tripping off when faults persist. Some have requirements on reactive power output during faults and active power output recovery speed after fault clearance.

A commonly adopted fault ride-through method in doubly-fed induction generator (DFIG)-based wind farms is a crowbar system, which mainly consists of resistors and switches [7]. A crowbar is connected between the rotor and the rotor converter. When faults happen in the grid, rotor currents would increase because of increased induced rotor voltages. The crowbar will then be switched on, and large currents from the rotor would flow into the crowbar rather than the rotor converter, thus protecting the rotor converter from being impacted by overcurrents [8]. Crowbar systems are simple and cheap, but DFIGs are rendered uncontrollable and act like squirrel-cage rotors after crowbar activation. They would absorb reactive power and suppress stator voltages during faults, making the main grid less resilient [9]. In addition to crowbars, other fault ride through methods for DFIGs include adding other versions of crowbar, i.e., series dynamic resistor [10], installing additional devices, e.g., dynamic voltage restorers [11] and current limiters [12], implementing customized control strategies, which usually require increasing rotor converters' voltage ratings [13], and designing new DFIG architectures, which are complex and need additional hardware [14].

As the first contribution of this paper, cooperative fault management (CFM) is designed to leverage power converters of nearby PV farms to help boost ride through capability of DFIG-based wind farms. As will be discussed in Section 2.1, the reason for large rotor currents and crowbar

E-mail address: p.zhang@stonybrook.edu (P. Zhang).

This work was supported in part by the National Science Foundation, USA, under Grants ECCS-2002897, CNS-2006828 and ECCS-2018492, and in part by Department of Energy, USA Grants DE-EE0009341. This work relates to Department of Navy award N00014-20-1-2858 issued by the Office of Naval Research. The United States Government has a royalty-free license throughout the world in all copyrightable material contained herein.

^{*} Corresponding author.

activation in DFIGs is the fast-changing rates of stator voltages, not the low voltages themselves. Based on this observation, CFM controls nearby PV farms to output voltages of less changing rates, as a way to buffer fast-changing voltages at fault locations. When subject to voltages of smaller changing rates, DFIGs are less likely to have crowbar activated. CFM, without installing extra hardware, leverages facility of other renewable energy to prevent crowbar switching, enables DFIGs' controllable and better power output, and boosts voltage recovery. This voltage buffer function works during both fault initiation and fault clearance, since voltages change the most at those two instants.

Proper coordination between renewable resources during the time between fault initiation and fault clearance can alleviate disturbance from renewable resources, improve system resilience and maintain renewable energy's own reliable operation [15]. Distributed optimization has been used to coordinate networked microgrids and renewable resources during faults for being configurable, preserving privacy and supporting plug-and-play [16,17]. Besides fault management, optimization has also been adopted within other aspects of power system dynamics analysis and control, such as outage detection [18], wind farm de-loading [19] and system stability with feedback optimization [20]. The concern over real-time requirements has yet to be addressed when optimization is applied in power system dynamics, because optimization needs much more computation to get reference values than usual feedback control. Optimization-based methods have only been demonstrated with software-in-the-loop simulation, whose simulation time is unrelated to real-world clock. Even though real-time simulation has been used to verify control methods for power system dynamics [21,22], those verified methods are mostly proportional-integral (PI) control and none is the optimization-based control method.

As the second contribution, this paper uses software-defined controllers and controller-in-the-loop real-time simulations to demonstrate that optimization-based CFM is able to output reference values around 60 ms. Distributed optimization is formulated in CFM during faults to coordinate various PV farms with different properties, e.g., with or without storage. In our hardware setup, the physical system, including the main grid, the wind farm and PV farms, is modeled in a RTDS simulator, and every PV farm has one computer to run its optimization algorithm. To shorten the time for CFM to output reference values, reference values will be sent to the RTDS simulators immediately after all subproblems finish at least one round of optimization, instead of waiting for all subproblems to converge. Reference values are suboptimal initially but would proceed towards optimal values as computation continues.

The remainder of this paper is organized as follows. Section 2 is formulation and methods of CFM . Section 3 gives a hardware setup for real-time simulation. Section 4 presents various case studies, including three-phase to ground faults, real-time performance analysis, scalability analysis, and three-phase to ground faults without CFM. Conclusions and future work are in Section 5.

2. Formulation and methods of CFM

CFM for PV farms and DFIG-based wind farms has three consecutive stages: voltage buffer, PV farms coordination, and voltage buffer. The first voltage buffer stage happens immediately after faults occur and endures about 1 cycle (16.67 or 20 ms). During this stage, PV farms are controlled to output slowly decreasing voltages so that the nearby DFIG-based wind farm experiences voltages of low changing rates and the possibility of crowbar activation is reduced. The second stage, PV farms coordination stage, lasts from the end of the first stage to faults clearance. In this stage, distributed and asynchronous optimization is used to coordinate PV farms to support the main grid and ensure PV farms' operation. The studied system has multiple PV farms and one wind farm. This design is motivated by some existing renewable projects, such as Long Island community microgrid in New York State [23] and Helena energy center in Texas [24]. The wind farm

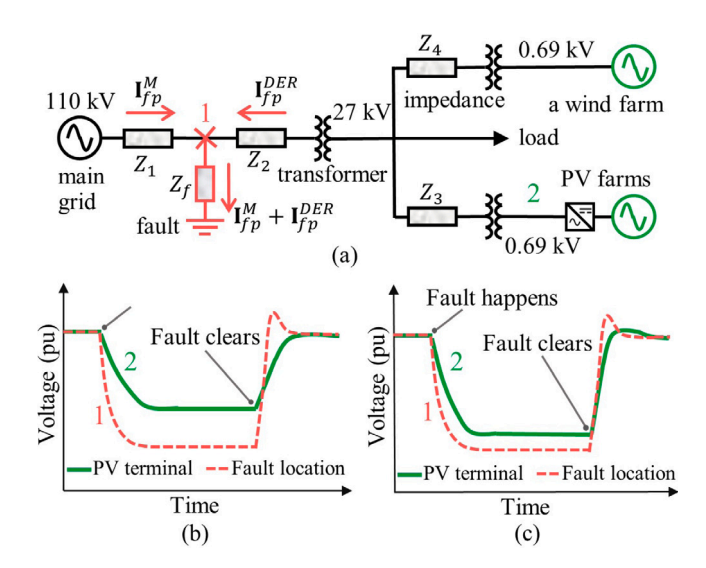


Fig. 1. Illustration of voltage buffer stage. (a) Schematic of studied system. Voltages at the fault location, indicated by 1, and at PV farms' terminal, indicated by 2, with voltage buffer (b) and without voltage buffer (c).

is controlled to output a large amount of reactive power in the second stage. The third stage, another voltage buffer stage, starts immediately after faults clear and endures about 1 cycle. PV farms are controlled to output slowly increasing voltages during the second voltage buffer stage.

2.1. Stage I: Voltage buffer

This subsection first describes the meaning of voltage buffer, then explains why voltage buffer works by analyzing DFIG fault characteristics, and lastly illustrates how voltage buffer is implemented in a control loop.

2.1.1. Rationale of voltage buffer

Fig. 1 illustrates of CFM's voltage buffer stage. After fault happens, voltages at the fault location, indicated by '1' in the figure, drop quickly. Fig. 1(b) and (c) show PV farms' output voltages with and without a voltage buffer, respectively. PV farms are chosen to implement voltage buffer function because they are connected to electrical grids through power converters. PV farms' outputs to the main grid are directly controlled by those highly controllable and fast converters. By contrast, a DFIG's stator is connected to the grid directly by power lines and its rotor is connected to the grid through a converter. The control of DFIGs' outputs to the grid is less direct and more complex.

With voltage buffer, PV farms are controlled to output voltages that decrease slower than fault location voltages. Since PV farms and the DFIG-wind farm are connected to the same Point of Connection (POC), DFIGs would experience slowly varying voltages. Slowly varying voltages decrease the probability of violating the rotor converter's capacity to maintain rotor currents below the crowbar's activation threshold. Large rotor currents are attributed to large changing rates of grid voltages, rather than to low voltage amplitudes. The faster the change of grid voltages, the larger the induced voltages on the DFIG rotor will be. If rotor voltages exceed rotor converters' voltage capacity, large rotor currents will appear. Then the crowbar will be activated and switched on, short-circuit rotor converters, direct large currents to the crowbar, and protect converters from overcurrents. Yet, crowbar activation renders DFIGs passive and poor power output.

Without voltage buffer, e.g., when PV farms are in power control mode, PV farms' output voltage would drop quickly after grid voltages drops, as shown in Fig. 1(c). DFIGs in the wind farm would then experience fast-changing voltages, followed by high induced voltages on the rotor, increased rotor currents and then crowbar activation.

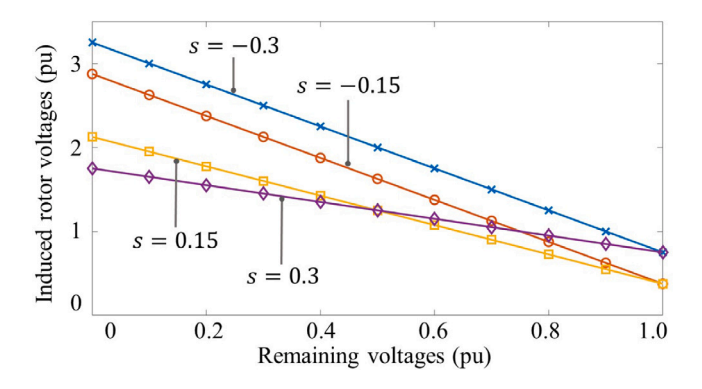


Fig. 2. Induced rotor voltages \mathbf{U}_r for different remaining voltages \mathbf{U}_{s1} and slip s during faults

2.1.2. DFIG fault characteristic

The DFIG model in a synchronously rotating d-q reference frame is expressed as [25],

$$\Psi_{s} = L_{s}\mathbf{I}_{s} + L_{m}\mathbf{I}_{r},\tag{1}$$

$$\Psi_r = L_r \mathbf{I}_r + L_m \mathbf{I}_s,\tag{2}$$

$$\mathbf{U}_{s} = R_{s}\mathbf{I}_{s} + \frac{d\boldsymbol{\Psi}_{s}}{dt} + jw_{s}\boldsymbol{\Psi}_{s},\tag{3}$$

$$\mathbf{U}_r = R_r \mathbf{I}_r + \frac{d\boldsymbol{\Psi}_r}{dt} + j(w_s - w_r) \boldsymbol{\Psi}_r, \tag{4}$$

where subscripts s and r indicate variables related to the stator and the rotor, respectively. L_m is the mutual inductance between the stator and rotor. $\Psi, \mathbf{I}, \mathbf{U}, w, R, L$ are flux linkage, current, voltage, electrical angular velocity (rad/s), resistance and inductance, respectively. The vectors in (1)–(4), i.e., $\Psi, \mathbf{I}, \mathbf{U}$, are expressed as, $\mathbf{A} = A_d + jA_q$.

Eqs. (1)–(4) are used to compute the rotor voltages U_r needed to maintain rotor currents I_r from increasing beyond crowbar threshold. First, solve for I_s in (1) and substitute the expression for I_s in (2). Then substitute the expression for Ψ_r in (4) to get the following,

$$\mathbf{U}_{r} = R_{r} \mathbf{I}_{r} + L_{r} L_{\delta} \frac{d\mathbf{I}_{r}}{dt} + \frac{L_{m}}{L_{s}} \frac{d\mathbf{\Psi}_{s}}{dt} + jsw_{s} (L_{r} L_{\delta} \mathbf{I}_{r} + \frac{L_{m}}{L_{s}} \mathbf{\Psi}_{s}), \tag{5}$$

where $L_{\delta}=1-\frac{L_m^2}{L_sL_r}$, and $s=\frac{w_s-w_r}{w_s}$ is rotor slip of DFIG and commonly in the range of [-0.3, 0.3]. Usually, R_r and L_{δ} are small and can be considered to be 0 for simplicity. Since \mathbf{I}_r is assumed to be always below crowbar activation threshold in this analysis, $\frac{d\mathbf{I}_r}{dt}$ is considered to be small and neglected. With the above assumptions, (5) can be expressed as,

$$\mathbf{U}_{r} = \frac{L_{m}}{L_{s}} \frac{d\boldsymbol{\Psi}_{s}}{dt} + jsw_{s} \frac{L_{m}}{L_{s}} \boldsymbol{\Psi}_{s}. \tag{6}$$

In (3), ignoring R_s , we can get expression for Ψ_s for a short time period Δt ,

$$\Psi_{s} = \frac{\mathbf{U}_{s0} - \mathbf{U}_{s1}}{jw_{s}} e^{-jw_{s}t} + \frac{1}{jw_{s}} \mathbf{U}_{s1}, \quad t \in [0, \Delta t],$$
 (7)

where \mathbf{U}_{s0} and \mathbf{U}_{s1} are stator voltages \mathbf{U}_{s} at time $t=0^{-}$ and $t=0^{+}$, respectively.

In normal conditions, e.g., without faults occurrence or faults clearance, $\mathbf{U}_{s0} = \mathbf{U}_{s1}$, the induced rotor voltage is,

$$\mathbf{U}_r = s \frac{L_m}{L_s} \mathbf{U}_s. \tag{8}$$

During faults occurrence or faults clearance at instant t = 0, $\mathbf{U}_{s0} \neq \mathbf{U}_{s1}$, the induced rotor voltage is,

$$\mathbf{U}_{r} = \frac{L_{m}}{L_{s}} \mathbf{s} \mathbf{U}_{s1} + \frac{L_{m}}{L_{s}} (s - 1)(\mathbf{U}_{s0} - \mathbf{U}_{s1}) e^{-jw_{e}t}, \tag{9}$$

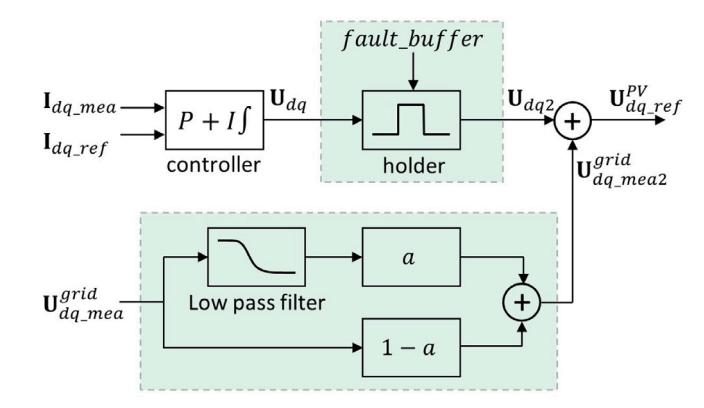


Fig. 3. Implementation of voltage buffer stage for a PV farm. Function blocks in the two dashed and shadowed areas are added to the traditional dq synchronous frame controller to realize voltage buffer function.

$$\|\mathbf{U}_r\| \le \frac{L_m}{L_s} \|s\mathbf{U}_{s1}\| + \frac{L_m}{L_s} \|(s-1)(\mathbf{U}_{s0} - \mathbf{U}_{s1})\|. \tag{10}$$

Fig. 2 shows the maximum possible $\|\mathbf{U}_r\|$ for different remaining voltages \mathbf{U}_{s1} and slip s, assuming $\mathbf{U}_{s0}=1$ pu and the rated rotor voltage is $s\frac{L_m}{L_s}\mathbf{U}_s=0.4\frac{L_m}{L_s}\mathbf{U}_s$, based on (8). It can be seen that the larger state voltages change, i.e., the smaller remaining voltages are, the larger the induced rotor voltages are. When induced rotor voltages \mathbf{U}_r exceed DFIG rotor converter's capacity, around 1.5 pu, rotor currents \mathbf{I}_r would increase and the crowbar will be activated.

2.1.3. Implementation of voltage buffer

Fig. 3 shows the implementation of voltage buffer stage. The two dashed and shadowed areas represent added function blocks to realize voltage buffer function. Without those blocks, the control scheme is the widely used dq synchronous frame controller [26,27]. In Fig. 3, the reference value for a PV farm's output voltage, $\mathbf{U}_{dq,ref}^{PV}$, is the sum of $\mathbf{U}_{dq,mea}^{grid}$ and \mathbf{U}_{dq2} . The measured grid voltage is $\mathbf{U}_{dq,mea}^{grid}$. PI controller's output, \mathbf{U}_{dq} , is the additional voltage needed to get the PV farm's reference current, $\mathbf{I}_{dq,ref}$. The measured current of the PV farm is $\mathbf{I}_{dq,mea}$. Signal f ault_buf f er is 1 when the PV farm is in voltage buffer stage and is 0 otherwise.

The voltage buffer stage is aimed to buffer voltage changes when large disturbances occur in the grid. The first added function block is a holder for the PI controller, freezing and keeping the controller's outputs unchanged following faults inception. This means \mathbf{U}_{dq2} would not change during voltage buffer stages. The second function block is to buffer $\mathbf{U}_{dq,mea}^{grid}$. In stable operations, $\mathbf{U}_{dq,mea}^{grid}$ are constants. Variable $a \in [0,1]$ decides the buffer level. When a=0, there is no buffer for $\mathbf{U}_{dq,mea}^{grid}$, and $\mathbf{U}_{dq,mea2}^{grid}$, equivalent to $\mathbf{U}_{dq,mea}^{grid}$, would drop quickly. When a=1, after fault happens, $\mathbf{U}_{dq,mea}^{grid}$ would drop quickly, but $\mathbf{U}_{dq,mea2}^{grid}$ would drop at a slower rate because of the low pass filter. A larger a results in slower change of $\mathbf{U}_{dq,ref}^{PV}$ but larger $\mathbf{I}_{dq,mea}$. For this reason, a should be large enough to buffer the PV farm's output voltages but should be small enough to maintain the PV farm's output currents within safety ratings.a is chosen to be about 0.5 in this paper.

The reason why a holder is used after U_{dq} while a low pass filter is used after $U_{dq,mea}^{grid}$ is that U_{dq} is the output of PI controllers and would change more unpredictably during transient dynamics. A holder can perform better than a low pass filter. In normal operations, U_{dq} is usually around 5% of $U_{dq,mea}^{grid}$. A holder cannot be used to buffer $U_{dq,mea}^{grid}$ because large currents would be induced with a holder, putting PV farms' converters at risk.

2.2. Stage II: PV farms coordination

CFM's second stage, PV farms coordination stage, is formulated as an optimization problem. Optimization formulation takes various variables into consideration and achieves better trade-offs between multiple objectives and constraints. Optimization brings flexibility, as objectives and constraints can be modified easily as needed.

The optimization of PV farms coordination stage is solved by distributed and asynchronous surrogate Lagrangian relaxation (DA-SLR), a method with mathematically proved convergence [28,29]. Distributed and asynchronous computation supports plug-and-play, preserves privacy and exploits local computation.

2.2.1. Optimization formulation

The objective has two parts, as shown in (11). The first part is a fault-current contributions, the differences between fault currents from the main grid and the total fault currents. Fault current contributions being zero means the integration of PV farms and wind farms has minimal effect on fault currents and thus causes little disturbance on the hosting grid. The second part is reactive power output, a large amount of which can boost voltages during faults and speed up system recovery from faults.

Voltages and currents are expressed in the complex plane and represented by complex vectors. Decision variables in this optimization formulation are each PV farm's currents, \mathbf{I}_i^{PV} , with each PV farm having six decision variables, each phase current represented by an imaginary part and a real part.

$$\min \ \left\{ \alpha_0 \sum_{fp} \left| \frac{[\text{Re}(\mathbf{I}_{fp}^M + \mathbf{I}_{fp}^{DEN})]^2 + [\text{Im}(\mathbf{I}_{fp}^M + \mathbf{I}_{fp}^{DEN})]^2}{[\text{Re}(\mathbf{I}_{fp}^M)]^2 + [\text{Im}(\mathbf{I}_{fp}^M)]^2} - 1 \right| - \sum_i \alpha_i Q_i^{PV} \right\},$$

where subscripts fp and i denote faulty phases and PV farms index, respectively. $fp \in \mathcal{P}(\{a,b,c\})$, power set of $\{a,b,c\}$. Superscripts M,DER,PV indicate variables related to the main grid, distributed energy resource (including both PV farms and the wind farm), and a single PV farm, respectively. Superscripts wind,PVs, discussed in the next paragraph, indicate variables related to the wind farm and summative variables of all PV farms, respectively.

Variables α_0 , α_i are weight factors. \mathbf{I}_{fp}^{M} , \mathbf{I}_{fp}^{DER} are fault currents from the main grid and from distributed energy, respectively. $\mathbf{I}_{fp}^{DER} = \mathbf{I}_{fp}^{wind} + \mathbf{I}_{fp}^{PVs}$, and $\mathbf{I}_{fp}^{PVs} = \sum_i \mathbf{I}_{i,fp}^{PV}$. Q_i^{PV} are reactive power output from PV farm i. Symbols Re and Im mean the real part and the imaginary part of complex numbers, respectively.

CFM's constraints can be put into two categories: coupling constraints and local constraints. Coupling constraints contain decision variables of more than one PV farm. Local constraints only involve decision variables of one PV farm. In the following constraints, (12)–(15), index i = 1...N with N being the number of PV farms. Phase j = a, b, c denotes power systems' three phases.

Coupling constraint: safety ratings of the substation that connects renewable generators to the transmission system. This means the sum of all PV farms' output currents, $\mathbf{I}_{j}^{PVs} = \sum_{i} \mathbf{I}_{i,j}^{PV}$, should be less than a safety threshold, $I^{S,PVs}$:

$$[\operatorname{Re}(\mathbf{I}_{i}^{PVs})]^{2} + [\operatorname{Im}(\mathbf{I}_{i}^{PVs})]^{2} \le (I^{S,PVs})^{2}.$$
 (12)

Local constraint 1: safety current ratings of each PV farm. Each PV farm's output currents should be less than its own safety threshold, $I_i^{S,PV}$:

$$[\operatorname{Re}(\mathbf{I}_{i,j}^{PV})]^2 + [\operatorname{Im}(\mathbf{I}_{i,j}^{PV})]^2 \le (I_i^{S,PV})^2. \tag{13}$$

Local constraint 2: sum of each PV farm's three-phase currents being zero. This constraint is required if a PV farm's interface converter is three-legged or if the transformer' winding at the PV farm side has no ground connection:

$$\sum_{j} \mathbf{I}_{i,j}^{PV} = \mathbf{0}. \tag{14}$$

Local constraint 3: power balance, which means a PV farm's active output power during faults should be the same as before faults. If a PV farm has no battery installed, this constraint is required; otherwise, this constraint is not needed. Power balance constraint is to protect PV farms and nearby grid networks from further disturbance caused by a large change in power flow:

$$P_i^{PV} = P_i^{req}. (15)$$

As explained, the above local constraint 2 and local constraint 3 do not necessarily apply to every PV farm. Their existence depends on individual PV farms' properties. This inclusion of various PV farm properties matches reality better, since PV farms are expected to be owned by different holders and possess distinct characteristics.

2.2.2. Distributed and asynchronous solutions

DA-SLR is used to decompose the above centralized formulation into multiple subproblems, with each PV farm having a subproblem. Specifically, the coupling constraint (12) is relaxed with Lagrangian multiplier vector λ and then the formulation is decomposed into N subproblems. Those subproblems are then computed in a distributed and asynchronous way. DA-SLR is proved mathematically to converge. It enables CFM's distributed computation, plug-and-play and privacy preservation.

Subproblem i, formulated and solved for PV farm i, is shown as follows:

$$\min \ \alpha_0 \sum_{fp} \left| \frac{[\text{Re}(\mathbf{I}_{fp}^M + \mathbf{I}_{fp}^{DER})]^2 + [\text{Im}(\mathbf{I}_{fp}^M + \mathbf{I}_{fp}^{DER})]^2}{[\text{Re}(\mathbf{I}_{fp}^M)]^2 + [\text{Im}(\mathbf{I}_{fp}^M)]^2} - 1 \right| - \alpha_i Q_i^{PV} + \lambda^T \mathbf{g}$$
 (16)

where whether constraint (14) or (15) is included depending on PV farm *i*'s technical specifications, $\lambda = [\lambda_a, \lambda_b, \lambda_c]$, $g = [g_a, g_b, g_c]$, with g_i (j = a, b, c) given in (18) after relaxation of coupling constraint (12):

$$g_{i} = [\text{Re}(\mathbf{I}_{i}^{PVs})]^{2} + [\text{Im}(\mathbf{I}_{i}^{PVs})]^{2} - (I^{S,PVs})^{2}.$$
(18)

During the computation, the coordinator, which can be an independent system operator (ISO), regional transmission organization (RTO), utility, distribution system operator (DSO) or transmission system operator (TSO) in reality, sends currents and Lagrangian multipliers to all PV farms. Then, each PV farm optimizes based on (16) and (17). Any PV farm that finishes its optimization would send its result to the coordinator. The coordinator then updates λ asynchronously and sends the updated multiplier values back to the PV farm. After that, PV farms would optimize based on updated values. The coordinator updates Lagrangian multipliers asynchronously based on the following equation:

$$\lambda^{k+1} = \lambda^k + d^k \mathbf{g}^k. \tag{19}$$

where k is the iteration number on the coordinator side, i.e., the kth time the coordinator updates λ . d^k , g^k are step size and relaxed constraints at iteration k, respectively. The above process repeats until convergence. Convergence criteria can be the change of variables, e.g., objective functions or decision variables, being smaller than preset thresholds. For the case study in Section 4, reference values are sent to PV farms after each distributed controller finishes at least one round optimization. This is to shorten the time of outputting reference values to meet real-time requirements.

2.3. Stage III: Voltage buffer

CFM's third stage is another voltage buffer stage, which starts immediately after faults clearance and endures about 1 cycle. When faults are cleared, by relays, circuit breakers or conductors breaking down, voltages can increase quickly [30]. When quickly decreasing or

(11)

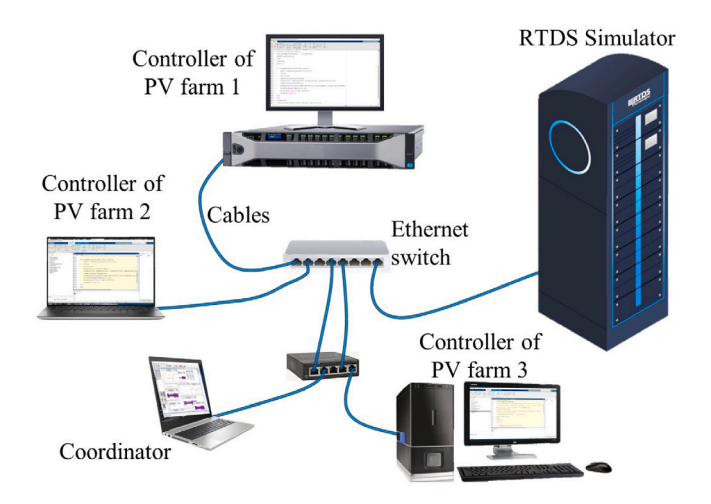


Fig. 4. Schematic of hardware setup for real-time simulation. RTDS: Real Time Digital

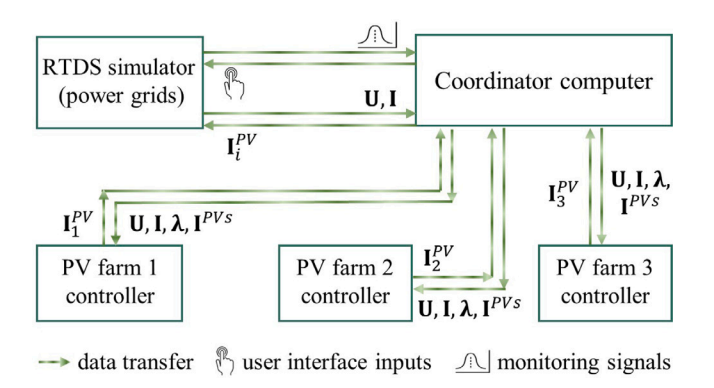


Fig. 5. Data transfer in real-time simulation.

increasing voltages are imposed on the DFIG-based wind farm, large currents in the rotor are induced and the crowbar is activated.

The green lines, indicated by 2, in Fig. 1(b) and Fig. 1(c) give the schematic of PV farms' output voltages during fault clearance with voltage buffer and without voltage buffer, respectively. The implementation of the voltage buffer stage during fault clearance is the same as the voltage buffer during fault inception, and is shown in Fig. 3.

3. Real-time simulation setup

This section explains the simulation setup with a real-time digital simulator. As discussed in Section 2.2, distributed optimization is used to coordinate multiple PV farms. One concern over applying optimization to power system dynamics is whether controllers can output reference values fast enough to meet real-time performance requirements. Without real-timeliness, developed algorithms cannot be used in actual implementations.

Fig. 4 shows the schematic of hardware setup for real-time simulation. This setup belongs to controller hardware-in-the-loop [31], because physical controllers have been connected to real-time simulators by I/O ports or network. The physical system, i.e., PV farms, the wind farm and other parts of power grids, is simulated in a simulator from RTDS Technologies [32]. One personal computer or server exclusively runs one PV farm's control algorithm. Another computer acts as the coordinator and is also used for monitoring and displaying real-time values. All the controller computers, the coordinator computer and the real-time simulator are connected to the network by cables and routers.

Fig. 5 shows the data transfer in real-time simulation. During faults, the RTDS simulator sends voltage signals U and current signals I,

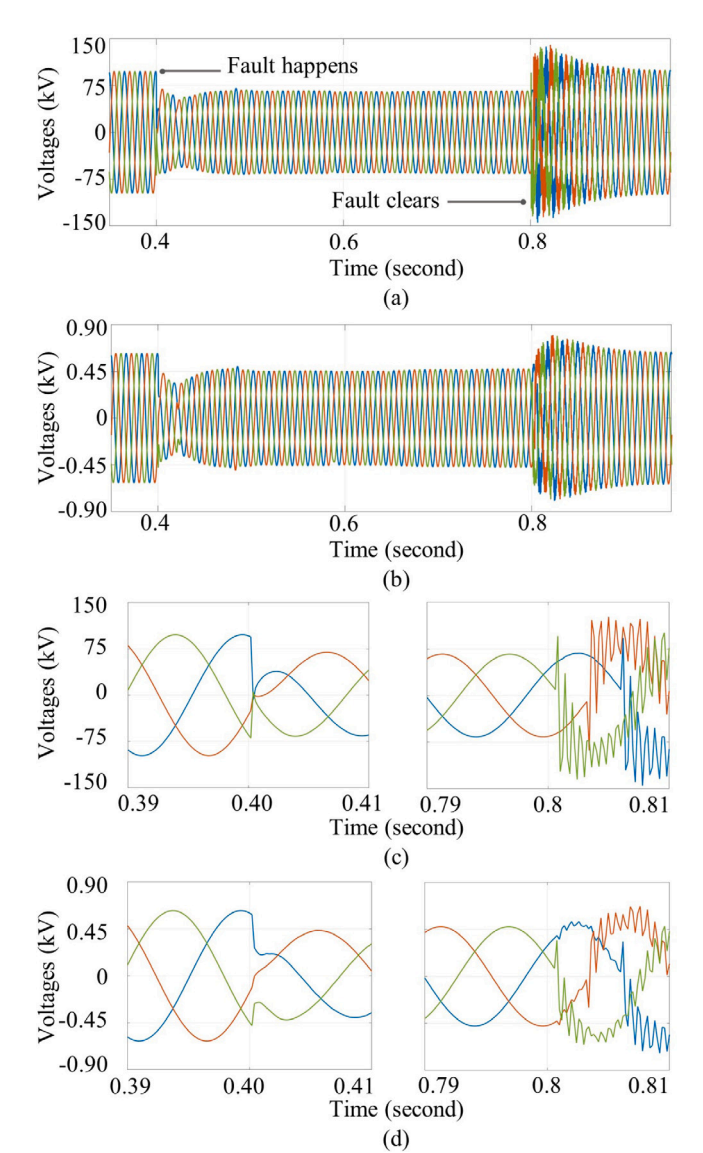


Fig. 6. Results for three-phase to ground faults, happening at 0.4 s and clearing at 0.8 s. (a) Voltages at the fault location. (b) Voltages at PV farms' terminal. (c) Zoomed-in version of subfigure (a). (d) Zoomed-in version of subfigure (b).

e.g., PV farms' terminal voltages and currents at the fault location, to the coordinator computer. The coordinator computer sends voltage signals, current signals, multipliers λ and sum of all PV farms' currents \mathbf{I}^{PVs} to all PV farms' controllers. Then, each PV farm's controller optimizes distributedly, gets their reference values \mathbf{I}_{i}^{PV} , and sends \mathbf{I}_{i}^{PV} to the coordinator computer. The coordinator computer sends reference values to the RTDS simulator so that PV farms output reference values. The coordinator computer then updates multipliers asynchronously and sends the latest parameters, i.e., U, I, λ, I^{PVs} , to distributed controllers, which would start next round optimization with newly received data after finishing their ongoing optimization. This communication and computation process repeats until fault clearance. During simulation, variables of interest, whether they are used in the optimization, are sent from the simulator to the coordinator computer for monitoring and displaying. Commands are sent from the coordinator to RTDS simulator, e.g., refreshing and transmission rate.

To meet real-time requirements, after every subproblem or controller finishes at least one round optimization, new reference values of all subproblems will be sent to the RTDS simulator. In this way, the real-time simulator would get reference values quickly. One round

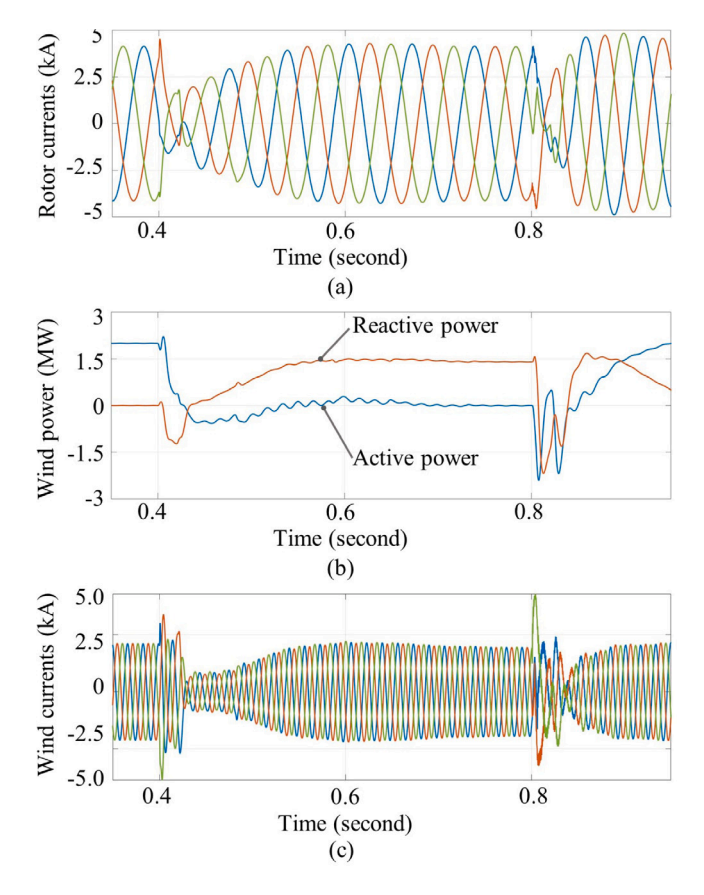


Fig. 7. Results for three-phase to ground faults. (a) Rotor currents, (b) output power of the DFIG-based wind farm and (c) wind farm output currents.

optimization of a subproblem starts when a distributed controller receives updated variable values and ends when the subproblem outputs its optimization results, i.e., decision variables. Even though those references are suboptimal initially, they would move towards optimal as computation proceeds, because the sent references are used as initial values for the next round optimization. It usually takes at least several rounds per controller for distributed optimization to converge, with the number of rounds depending on stopping criteria, initial values, coordination methods, and so on. However, it usually takes more than 200 ms for distributed optimization to converge this way, failing real-time requirements for power grids' fault management.

In Fig. 5, computations in the coordinator computer and all PV farms' controllers are conducted in software Matlab. TCP/IP protocol is used for the communication between the Matlab and the RTDS simulator. The RTDS simulator is designated as TCP server in its GTNET-SKT module, and the Matlab is designated as TCP client by its command tcpclient. User Datagram Protocol (UDP) is used for the communication between Matlab sections in different computers, i.e., the coordination computer and each PV farm's controller computer, with command udpport being used. The coordination computer needs to set multiple UDP local ports, three in this paper, and each PV farm's controller only needs one UDP local port.

4. Case study

This section presents real-time simulation results with the hardware setup shown in Fig. 4. Four computers have been used: a DELL PowerEdge R740, a Dell Precision 7750, a Dell Precision 5820 and an ASUS K501U. Three PV farms are simulated in the RTDS NOVACOR simulator. Every PV farm has one computer run its optimization algorithm, and the fourth computer acts as the coordinator. The adjustable RTDS

sample time is set to 20 ms in this paper. Magnitudes and angles of voltage and current vectors are sent to controllers.

The schematic of the simulated system in the RTDS simulator is shown in Fig. 1. One wind farm and three PV farms have been simulated. The main grid is of 110 kV and connected to the 27 kV distribution system by a transformer. The wind farm and PV farms are connected to the 27 kV distribution system by transformers with voltage ratings of 27 kV/0.69 kV. The terminal voltage ratings for both wind and PV generations are 0.69 kV. $Z_1 = 50.83 + j384.5 \Omega$, $Z_2 = 25.42 + j192.26 \Omega$ and $Z_3 = Z_4 = 1.53 + j5.74 \Omega$. These impedance values are chosen to represent about 5% voltage drop. PV farm 1, PV farm 2 and PV farm 3 have capacities of 3.0 MW, 4.0 MW and 2.0 MW, respectively. The three PV farms output 1.2 MW, 1.8 MW and 1.0 MW before faults, respectively, all with power factor 1.0. PV farm 1 and PV farm 3 have storage, so constraint (15) does not exist in their formulation during the PV farms coordination stage. PV farm 2 does not have storage and thus constraint (15) exists in its formulation. The wind farm is of 2.0 MW capacity and outputs 2.0 MW active power and 0.0 MW reactive power before faults. The wind farm is modeled as a DFIG, rotating at 45 Hz before faults, i.e., slip s = 0.25.

4.1. Three-phase to ground faults with CFM

A three-phase to ground fault happens at the 110 kV line at 0.4 s and clears at 0.8 s with the grounding resistance $Z_F = 325.0 \,\Omega$, as shown in Fig. 1. Fig. 6 shows voltages at the fault location and PV farms' terminal, indicated by number 1 and 2 respectively in Fig. 1. The first and second buffer stages span from 0.40 s to 0.42 s and from 0.80 s to 0.82 s, respectively. Fig. 6(c) and (d) are the zoomedin versions of Fig. 6(a) and (b), respectively. During fault inception and clearance, because of the voltage buffer stage in CFM, voltages at PV farms terminal change slower than voltages at the fault location. Specifically, from 0.400 s to 0.401 s, phase a has the largest voltage change, and instant phase a voltage at the fault location drops from 94.60 kV to 25.22 kV, a 70.88% drop compared with voltage amplitude 97.88 V. By contrast, instant phase a voltage at PV farms terminal drops from 588.9 V to 201.1 kV, a 62.02% drop compared with voltage amplitude 625.3 V. From 0.400 s to 0.401 s, instant phase a voltage at the fault location has the largest voltage drop to -7.822 kV at 0.4004 s, a 104.6% drop. Contrarily, phase a voltage at PV farms terminal has the largest drop of 62.02% at 0.401 s from 0.400 s to 0.401 s.

As shown in (10) and Fig. 2, for DFIG-based wind farms, larger grid voltage difference induces large rotor voltages and thus requires rotor converters to output larger voltages to control rotor currents. When the required voltages exceed rotor voltage capacity, large rotor currents would appear and activate the crowbar. Fig. 7 shows the DFIG's rotor currents and output power. Because of the voltage buffer implemented with PV farms' interface converters, the DFIG, connected to the same collector substation with PV farms, experiences voltages of less changing rates. During fault inception and fault clearance, the rotor currents remain below the crowbar's activation threshold, set as 1.3 times rated currents. With the crowbar not being activated, the DFIG-based wind farm keeps synchronized and controllable, and it is controlled to output a large amount of reactive power to support voltage recovery.

From 0.42 s to 0.80 s is the PV farms coordination stage. The objective function in (11) has two parts: fault current contributions and reactive power output. Fig. 8(a) shows root-mean-square (RMS) amplitude differences between total fault currents to the ground and fault currents from the main grid. At 0.417 s, the fault current difference reaches its largest at 65.75 A, meaning that PV and wind farms contribute to the increase of the total fault currents by 65.75 A. As PV farms coordination proceeds, current differences, i.e., fault current contributions from renewable energy, reduce gradually to zero. Fig. 8(b) shows output power of PV farm 1, which has batteries and thus no requirement on active power balance constraint (15). PV farm 1 is

managed to output reactive power as much as possible. Fig. 8(c) shows output power of PV farm 2, which has no battery and thus is required to satisfy active power balance constraint (15). PV farm 2 is managed to output the same amount of active power before fault and also to output maximum possible reactive power. At some instants, e.g., 0.482 s, 0.586 s and 0.644 s, the output power of PV farm 2 changes relatively largely. This is because controllers send new reference values to RTDS simulators at those instants.

4.2. Real-time performance analysis

One concern for using optimization in power system dynamic control is computation time, which should be small enough to output reference values promptly. Fig. 9(a) is an optimization finishing sequence during fault management. Results in this subfigure belong to the same simulation case in the previous Section 4.1. In the simulation, every 20 ms, the RTDS simulator sends data to the coordinator controller. The sent data include an incremental number, incrementing by 1 every 20 ms, and system states, e.g., voltages and currents. After each PV farm's control has finished at least one round optimization, the coordinator computer sends reference values and the incremental number back to the RTDS simulator. The incremental number is not used in computations. It is used for calculating computation time.

When there is no fault or optimization computation, the coordinator controller can send received incremental numbers back to the RTDS simulator almost immediately. This forward and backward communication takes about 3.5 ms, which is why in Fig. 9(a), the bottom line lags the upper line by about 3.5 ms before fault and after a fault. During the PV farm coordination stage, from 0.42 s to 0.80 s, controllers have sent to the RTDS simulator the incremental number and reference values five times, at 0.4816 s, 0.5860 s, 0.644 s, 0.664 s and 0.728 s, respectively. Those five optimizations take 54.4 ms, 104.4 ms, 58.0 ms, 20.0 ms and 64.0 ms, respectively, averaging 60.16 ms. The last optimization lasts 94.0 ms, from 0.728 s to 0.822 s, but its reference values are not used, as the fault ends at 0.80 s.

Fig. 9(b) is the computation time of distributed optimization during PV farms coordination stage. The computation time includes communication time between the RTDS simulator and the coordinator controller, the time lapse for every PV farm to finish at least one round optimization, and communication time between the coordinator controller and PV farm controllers. The computation time in Fig. 9(b) averages 65.49 ms with a stand deviation of 37.47 ms. The results demonstrate that the proposed optimization-based PV farms coordination method is fast enough to output reference values for dynamic control. Hardware-in-the-loop simulations are closer to reality and related results are more convincing than software-in-the-loop.

4.3. Scalability analysis

In this subsection, the physical system has one wind farm and 24 PV farms, increased from 3 PV farms. Rather than using 24 computers as distributed controllers, 24 cores within one DELL PowerEdge R740 computer are used, with one core running one PV farm's control algorithm. The distributed and asynchronous computation with multiple cores is realized with *parfeval* command in Matlab's Parallel Computing Toolbox. The wind farm is of 2.0 MW capacity and runs at the rated capacity with a power factor of 1.0 before faults. The total capacity of the 24 PV farms is 9.0 MW and they output 4.0 MW active power and 0.0 MW reactive power before faults.

Fig. 10 shows simulation results with 24 PV farms. Subfigure (a) is the DFIG rotor currents, which are always below the crowbar activation threshold, 1.3 times rated currents. Without a crowbar being activated, the DFIG always keeps controllable. Subfigure (b) is the RMS amplitude differences between total fault currents to the ground and fault currents from the main grid. RMS amplitude differences represent fault current contributions from renewable resources. Fault current contributions

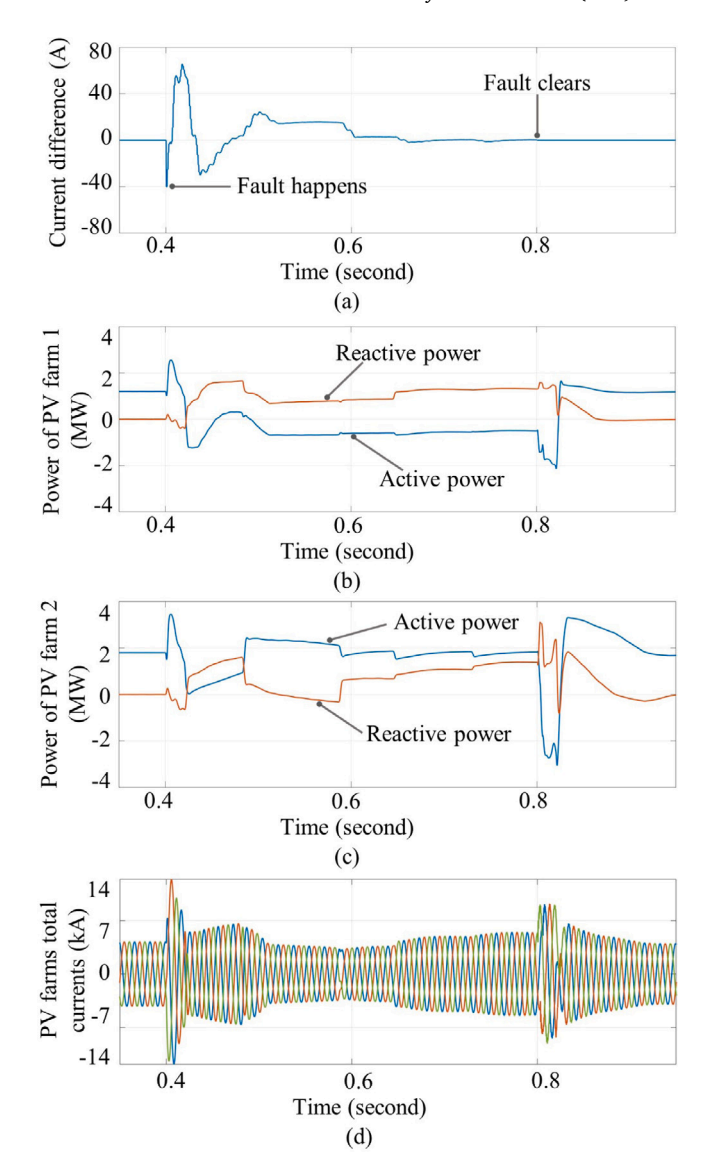


Fig. 8. Results for three-phase to ground faults. (a) RMS amplitude differences between total fault currents to the ground and fault currents from the main grid, expressed as $\|\mathbf{I}_{fp}^{M} + \mathbf{I}_{fp}^{DER}\| - \|\mathbf{I}_{fp}^{M}\|$. The amplitude differences represent the fault current contribution from distributed energy. Output power of (b) PV farm 1 and (c) PV farm 2. (d) Sum of all PV farms currents.

are reduced to zero during faults. Subfigure (c) is output power from renewable resources, including the wind farm and all 24 PV farms. One objective component during faults is to maximize reactive power output, which is why a large amount of reactive power is output by renewable resources. Subfigure (d) is the optimization finishing sequence during the PV farm coordination stage. Reference values have been sent to the RTDS simulator from the coordinator controller six times. The mean computation time of these six optimizations is 61.83 ms, and the standard deviation is 5.78 ms. The possible reason for a smaller standard deviation in multi-core implementation in Fig. 10 than the multi-PC implementation in Fig. 9 is that the communication between cores within one computer is more stable than the communication between multiple computers.

The results in Fig. 10 justify the potential of proposed PV farms coordination to be used to manage large numbers of heterogeneous PV farms during faults. One challenge for scaling up is the longer communication time between the coordinator and subproblems during

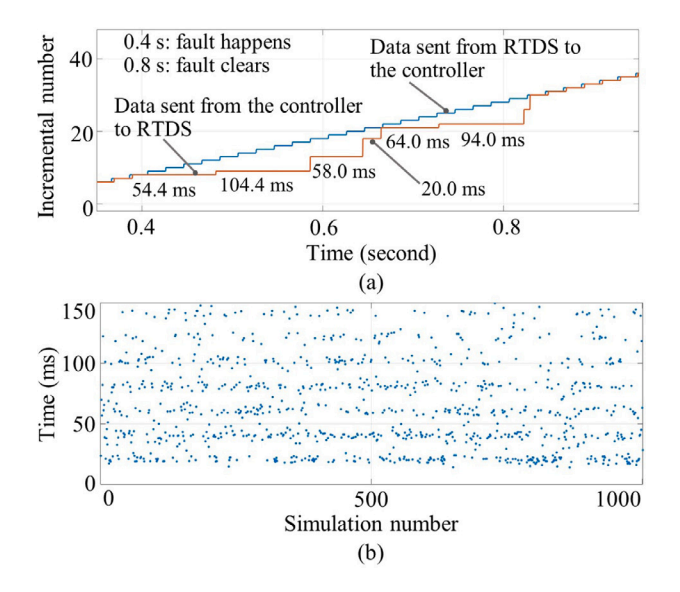


Fig. 9. Results for real-time performance analysis. (a) Optimization finishing sequence during fault management. (b) Computation time of PV farms coordination stage.

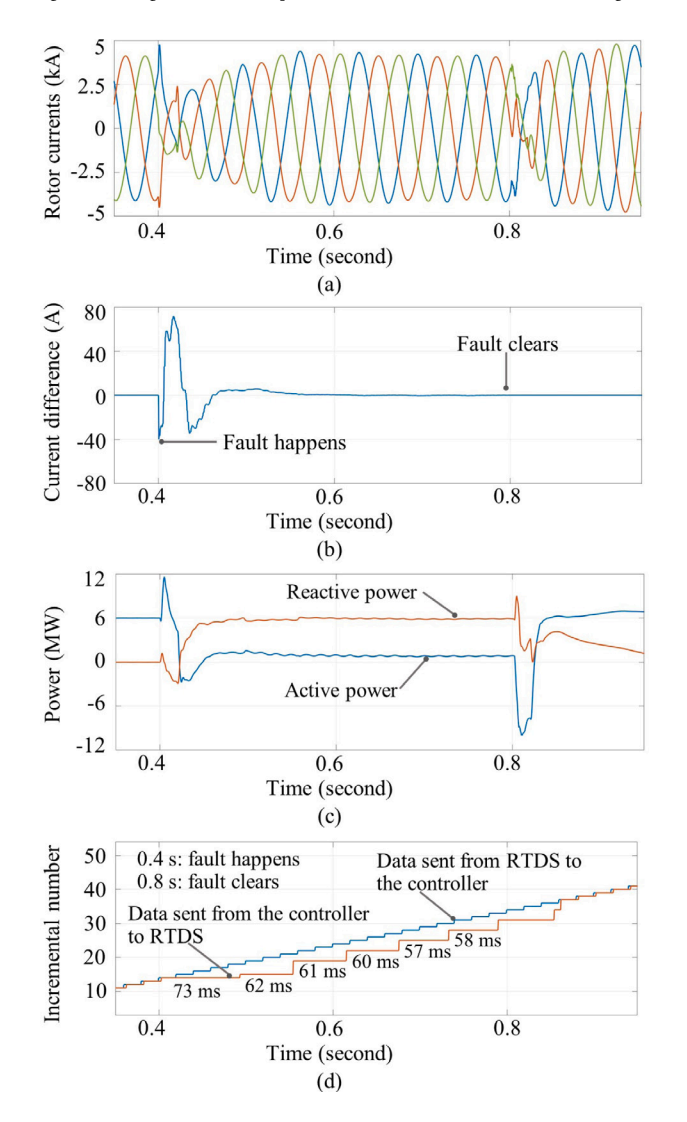


Fig. 10. Results for scalability analysis. (a) Rotor currents in DFIG-based wind farm. (b) The RMS amplitude differences between total fault currents to the ground and fault currents from the main grid. (c) Output power from renewable resources, including the wind farm and all PV farms. (d) Optimization finishing sequence.

distributed optimization. In our current experiment setup and implementation, when the coordinator is transferring data with one subproblem, it cannot have data transfer with other subproblems. For example, the coordinator computer can only send the multipliers to each subproblem computer one after another instead of simultaneously. As a result, more PV farms would increase communication time. If the coordinator computer can send multipliers simultaneously to all subproblems and also receive new results simultaneously from multiple subproblems, then scaling up to hundreds of PV farms with DA-SLR should be realizable.

4.4. Three-phase to ground faults without CFM

This section presents real-time simulation results without CFM, i.e., without voltage buffer or PV farms coordination. PV farms are in power control mode during faults, namely, maintaining the same power output within current ratings. A three-phase to ground fault happens at the 110 V section at 0.40 s and clears at 0.80 s with the grounding resistance $Z_F = 325 \,\Omega$, as shown in Fig. 1.

Fig. 11 shows simulation results without CFM. Fig. 11(a) is the total power of all PV farms, controlled to be the same as before faults. Without voltage buffer stage, immediately after fault inception and fault clearance, voltages at PV farms' terminals would change nearly as much as grid voltages. Specifically, from 0.400 s to 0.401 s, phase *a* has the largest voltage change and instant phase *a* voltage at PV farms terminal drops from 592.5 V to 162.7 kV, a 70.33% drop compared with voltage amplitude 625.3 V. The drop is similar to the voltage drop at the fault location, 70.88%, and larger than voltages drop at PV farms terminal with CFM, 62.02%.

Without voltage buffer, the DFIG, connected to the same collector substation with PV farms, experiences voltages of larger changing rates. As a result, rotor currents increase above the crowbar's activation threshold, set as 1.3 times rated currents, during both fault inception and fault clearance, and the crowbar is activated twice, as shown in Fig. 11(c) and (d). With the crowbar switching on and bypassing the rotor converter, the DFIG-based wind farm loses controllability and acts as an asynchronous motor, absorbing reactive power, as shown in Fig. 11(e). The wind farm absorbing reactive power is not desirable for voltage recovery. Fig. 11(f) shows the RMS amplitude differences between total fault currents to the ground and fault currents from the main grid. Without PV farms coordination, the current difference levels out at 37.97 A, meaning PV and wind farms contribute to increasing total fault currents by 37.97 A.

By comparison between real-time simulation results in Section 4.1 with CFM and the results in this subsection without CFM, it is concluded that with CFM's voltage buffer stage, the crowbar in the DFIG-based wind farm would not be activated, enabling the wind farm to be controllable all the time. The wind farm then can be controlled to output reactive power to help voltage recovery. Also, with CFM's PV farms coordination stage, PV farms can contribute to keeping the total fault currents and the fault currents from the main grid having the same amplitude, meaning renewable energy penetration causes less disturbance to the main grid.

5. Conclusion

CFM is developed to enable renewable energy resources' fault ridethrough capabilities and to improve power grid resilience, with different types of renewable resources cooperating with and complementing each other. Simulations demonstrate PV farms' power converters can assist nearby DFIG-based wind farms in riding through faults and that various renewable resources can coordinate to reduce disturbance and help boost recovery during faults. Real-time simulation results with controller hardware-in-the-loop justify the distributedoptimization-based CFM can output reference values quick enough, around 60 ms, for controlling power grid dynamics and be scaled up

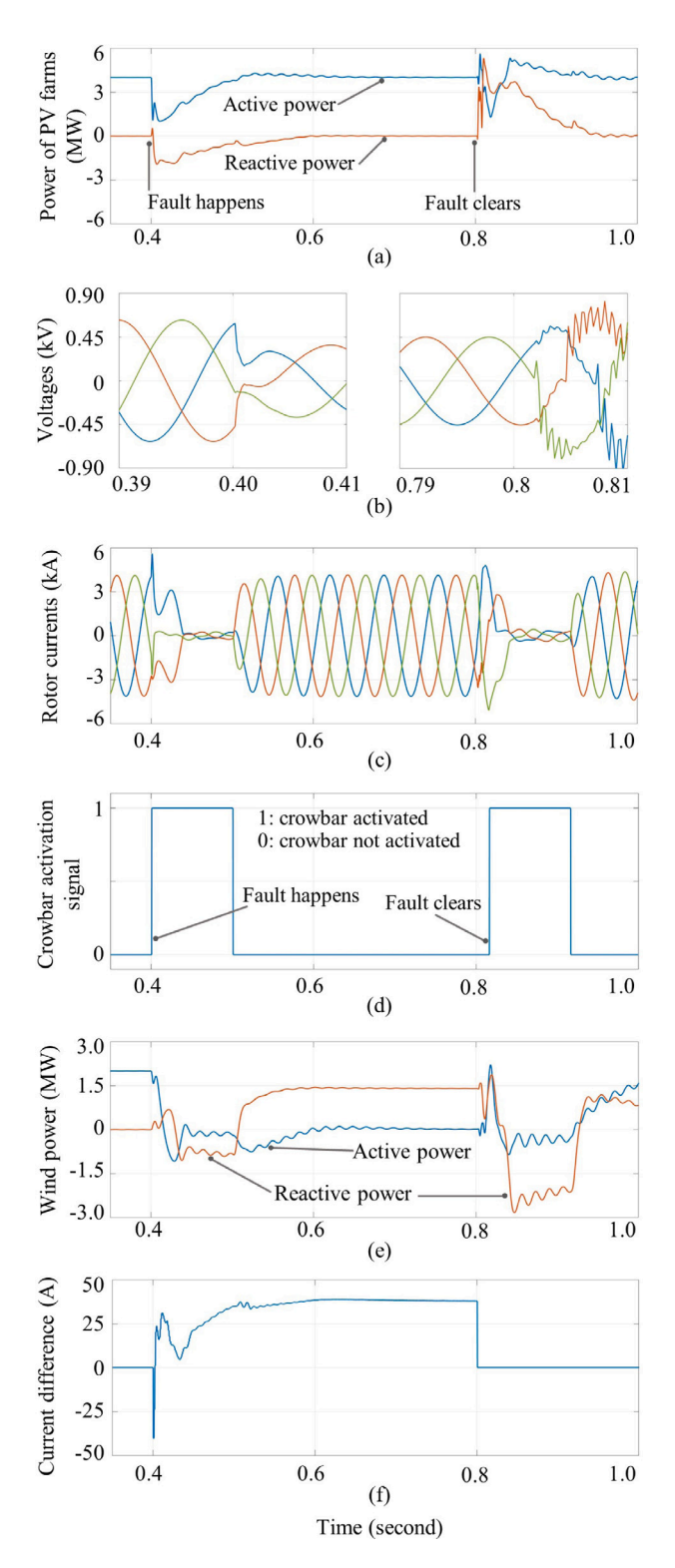


Fig. 11. Results without cooperative fault management. (a) Powers of all PV farms. (b) Voltages at PV farms' terminal. (c) Rotor currents of the DFIG-based wind farm. (d) Crowbar activation signal. (e) Power of the wind farm. (f) The RMS amplitude differences between total fault currents to the ground and fault currents from the main grid.

to a large number of renewable generators. CFM belongs to primary control and should be activated upon fault detection. The idea of cooperative and complementary management between PV and wind can be extended to other renewable energy. Fault management with

electric vehicle facilities and with large systems is in the future research plan.

CRediT authorship contribution statement

Wenfeng Wan: Algorithm design and software development, Analysis of results, Writing – original draft. Peng Zhang: Principal investigator, Supervision, Conceptualization, Methodology, Analysis, Manuscript preparation and editing. Mikhail A. Bragin: Algorithm design, Manuscript proofreading and editing. Peter B. Luh: Algorithm design, Writing – review & editing.

Declaration of competing interest

The authors declare that they have no known competing financial interests or personal relationships that could have appeared to influence the work reported in this paper.

References

- Google, Four consecutive years of 100% renewable energy and what's next, 2021,
 URL: https://cloud.google.com/blog/topics/sustainability/google-achieves-four-consecutive-years-of-100-percent-renewable-energy.
- [2] U.S. Energy Information Administration (EIA), Summary of Legislation and Regulations Included in the Annual Energy Outlook 2021, Technical Report, U.S. Department of Energy, 2020.
- [3] Energy Emergencies Executive Committee (E3C), Great Britain Power System Disruption On 9 August 2019, Technical Report, UK Department of Energy and Climate Change, 2020.
- [4] North American Electric Reliability Corporation (NERC), 1,200 MW Fault Induced Solar Photovoltaic Resource Interruption Disturbance Report, Technical Report, 2017.
- [5] IEEE standard for interconnection and interoperability of distributed energy resources with associated electric power systems interfaces, IEEE Std 1547-2018 (2018) 1–138, http://dx.doi.org/10.1109/IEEESTD.2018.8332112.
- [6] S. Probert, S. Nutt, Generator Fault Ride Through (FRT) Investigation: Literature Review, Technical Report, Transpower New Zealand Limited, 2009.
- [7] J. Morren, S. de Haan, Ridethrough of wind turbines with doubly-fed induction generator during a voltage dip, IEEE Trans. Energy Convers. 20 (2) (2005) 435–441, http://dx.doi.org/10.1109/TEC.2005.845526.
- [8] A. Rini Ann Jerin, P. Kaliannan, U. Subramaniam, M. Shawky El Moursi, Review on FRT solutions for improving transient stability in DFIG-WTs, IET Renew. Power Gener. 12 (15) (2018) 1786–1799.
- [9] G. Pannell, D.J. Atkinson, B. Zahawi, Minimum-threshold crowbar for a fault-ride-through grid-code-compliant DFIG wind turbine, IEEE Trans. Energy Convers. 25 (3) (2010) 750–759.
- [10] J. Yang, J.E. Fletcher, J. O'Reilly, A series-dynamic-resistor-based converter protection scheme for doubly-fed induction generator during various fault conditions, IEEE Trans. Energy Convers. 25 (2) (2010) 422–432.
- [11] C. Wessels, F. Gebhardt, F.W. Fuchs, Fault ride-through of a DFIG wind turbine using a dynamic voltage restorer during symmetrical and asymmetrical grid faults, IEEE Trans. Power Electron. 26 (3) (2010) 807–815.
- [12] G. Rashid, M.H. Ali, Nonlinear control-based modified BFCL for LVRT capacity enhancement of DFIG-based wind farm, IEEE Trans. Energy Convers. 32 (1) (2016) 284–295.
- [13] L. Yang, Z. Xu, J. Ostergaard, Z.Y. Dong, K.P. Wong, Advanced control strategy of DFIG wind turbines for power system fault ride through, IEEE Trans. Power Syst. 27 (2) (2011) 713–722.
- [14] P.S. Flannery, G. Venkataramanan, A fault tolerant doubly fed induction generator wind turbine using a parallel grid side rectifier and series grid side converter, IEEE Trans. Power Electron. 23 (3) (2008) 1126–1135.
- [15] P. Zhang, Networked Microgrids, Cambridge University Press, 2021.
- [16] W. Wan, M.A. Bragin, B. Yan, Y. Qin, J. Philhower, P. Zhang, P.B. Luh, Distributed and asynchronous active fault management for networked microgrids, IEEE Trans. Power Syst. 35 (5) (2020) 3857–3868, http://dx.doi.org/10.1109/ TPWRS.2020.2976044.
- [17] W. Wan, M. Bragin, P. Luh, P. Zhang, DA-AFM For ultra PV and wind energy integration, in: 2021 IEEE Power Energy Society General Meeting, PESGM, 2021.
- [18] X. Yang, N. Chen, C. Zhai, A control chart approach to power system line outage detection under transient dynamics, IEEE Trans. Power Syst. 36 (1) (2020) 127–135.
- [19] X. Fan, E. Crisostomi, D. Thomopulos, B. Zhang, R. Shorten, S. Yang, An optimized decentralized power sharing strategy for wind farm de-loading, IEEE Trans. Power Syst. 36 (1) (2020) 136–146.

- [20] S. Menta, A. Hauswirth, S. Bolognani, G. Hug, F. Dörfler, Stability of dynamic feedback optimization with applications to power systems, in: 56th Annual Allerton Conference on Communication, Control, and Computing, Allerton, 2018, pp. 136–143, http://dx.doi.org/10.1109/ALLERTON.2018.8635640.
- [21] L. Wang, Y. Qin, Z. Tang, P. Zhang, Software-defined microgrid control: The genesis of decoupled cyber-physical microgrids, IEEE Open Access J. Power Energy 7 (2020) 173–182, http://dx.doi.org/10.1109/OAJPE.2020.2997665.
- [22] X. Guillaud, M.O. Faruque, A. Teninge, A.H. Hariri, L. Vanfretti, M. Paolone, V. Dinavahi, P. Mitra, G. Lauss, C. Dufour, P. Forsyth, A.K. Srivastava, K. Strunz, T. Strasser, A. Davoudi, Applications of real-time simulation technologies in power and energy systems, IEEE Power Energy Technol. Syst. J. 2 (3) (2015) 103–115, http://dx.doi.org/10.1109/JPETS.2015.2445296.
- [23] Clean Coalition, Long Island Community Microgrid Project (LICMP), 2021, URL: https://clean-coalition.org/community-microgrids/long-island-community-microgrid-project/.
- [24] Helena Energy Center, 2021, URL: https://helenaenergycenter.com/.
- [25] L. Xu, P. Cartwright, Direct active and reactive power control of DFIG for wind energy generation, IEEE Trans. Energy Convers. 21 (3) (2006) 750–758, http://dx.doi.org/10.1109/TEC.2006.875472.

- [26] V. Blasko, V. Kaura, A new mathematical model and control of a three-phase AC-DC voltage source converter, IEEE Trans. Power Electron. 12 (1) (1997) 116–123, http://dx.doi.org/10.1109/63.554176.
- [27] M. Liserre, F. Blaabjerg, A. Dell'Aquila, Step-by-step design procedure for a grid-connected three-phase PWM voltage source converter, Int. J. Electron. 91 (8) (2004) 445–460.
- [28] M.A. Bragin, B. Yan, P.B. Luh, Distributed and asynchronous coordination of a mixed-integer linear system via surrogate Lagrangian relaxation, IEEE Trans. Autom. Sci. Eng. (2020) 1–15, http://dx.doi.org/10.1109/TASE.2020.2998048.
- [29] M.A. Bragin, P.B. Luh, J.H. Yan, N. Yu, G.A. Stern, Convergence of the surrogate Lagrangian relaxation method, J. Optim. Theory Appl. 164 (1) (2015) 173–201.
- [30] Y. Guan, W. Gao, W. Liu, N. Du, Z. Xiang, Overvoltages of 40.5 kV vacuum circuit breaker switching off shunt reactors, in: 2011 IEEE Power Engineering and Automation Conference, vol. 2, 2011, pp. 197–200, http://dx.doi.org/10. 1109/PEAM.2011.6134956.
- [31] M. Steurer, F. Bogdan, W. Ren, M. Sloderbeck, S. Woodruff, Controller and power hardware-in-loop methods for accelerating renewable energy integration, in: 2007 IEEE Power Engineering Society General Meeting, IEEE, 2007, pp. 1–4.
- [32] RTDS technologies, 2021, URL: https://www.rtds.com/.